Research Article Vol. 10, No. 6 / June 2022 / Photonics Research 1509

Monolithic GaAs/Si V-groove depletion-type optical phase shifters integrated in a 300 mm Si photonics platform

Younghyun Kim,[1,2,*] Didit Yudistira,[1] Bernardette Kunert,[1] Marina Baryshnikova,[1] Reynald Alcotte,[1] Cenk Ibrahim Ozdemir,[1] Sanghyeon Kim,[1,3] Sebastien Lardenois,[1] Peter Verheyen,[1] Joris Van Campenhout,[1] and Marianna Pantouvaki[1]

[1]IMEC, Heverlee B-3001, Belgium
[2]Current address: Department of Photonics and Nanoelectronics, BK21 FOUR ERICA-ACE Center, Hanyang University, Ansan 15588, Republic of Korea
[3]Current address: School of Electrical Engineering, Korea Advanced Institute of Science and Technology (KAIST), Daejeon 34141, Republic of Korea
*Corresponding author: younghyunkim@hanyang.ac.kr

Received 21 December 2021; revised 15 March 2022; accepted 30 March 2022; posted 31 March 2022 (Doc. ID 451821); published 26 May 2022

We demonstrate monolithically integrated n-GaAs/p-Si depletion-type optical phase shifters fabricated on a 300 mm wafer-scale Si photonics platform. We measured the phase shifter performance using Mach–Zehnder modulators with the GaAs/Si optical phase shifters in both arms. A modulation efficiency of $V_\pi L$ as low as 0.3 V·cm has been achieved, which is much lower compared to a carrier-depletion type Si optical phase shifter with pn junction. While propagation loss is relatively high at ∼6.5 dB/mm, the modulator length can be reduced by the factor of ∼4.2 for the same optical modulation amplitude of a Si reference Mach–Zehnder modulator, owing to the high modulation efficiency of the shifters.

https://doi.org/10.1364/PRJ.451821

1. INTRODUCTION

Optical phase shifters are one of the key components in integrated photonics, enabling the control of optical signals by manipulating the phase of light. They have been optimized for more than a decade in the context of the development of high-speed Si Mach–Zehnder modulators (MZMs), for which they are an essential building block [1,2].

Si MZMs have been demonstrated with high-speed modulation and broad bandwidth, but they still suffer from a relatively large device footprint of several millimeters, due to the insufficient electro-optic effect in Si [3,4]. Heterogeneous III–V integration in conjunction with a Si photonics platform has been introduced not only for the lasers but also for the modulators [5–11] in order to address the mentioned problem, leveraging the greater carrier-induced change in refractive index in III–V materials compared to Si [12]. The demonstrated heterogeneous III–V/Si modulators are typically fabricated through die-to-wafer bonding with ultra-thin bonding layers (<10 nm) and require metal contacts to the III–V material to realize the desired III–V-insulator-Si capacitive phase shifter structures. The fabrication steps are quite challenging and less CMOS compatible, which may result in lower manufacturability and scalability.

Integration of the III–V on the Si platform through monolithic hetero-epitaxy has been investigated for the next-generation electronic and photonic devices in a CMOS pilot line [13,14]. Recently, optically pumped lasing has been demonstrated from monolithic III–V waveguides on Si [15,16]. In addition, we have proposed the bonding-free III–V/Si optical phase shifter and investigated its performance by using technology computer-aided design (TCAD) simulations, resulting in outperforming optical loss as well as modulation efficiency compared to conventional Si optical phase shifters [17,18].

In this paper, we report the experimental demonstration of the GaAs/Si depletion-type optical phase shifter, leveraging the direct growth of GaAs on a Si V-groove and its performance. To the best of our knowledge, this is the first demonstration of the monolithic integration of a III–V on a Si photonic platform for optical phase shifters featuring a high modulation efficiency of 0.3 V · cm, which is 2.5 times lower than the Si baseline.

2. DEVICE DESIGN AND FABRICATION

First, we show the schematic of an MZM, which mainly consists of Si optical waveguides and the GaAs/Si optical phase shifter in both arms in Fig. 1(a). The cross-section of the

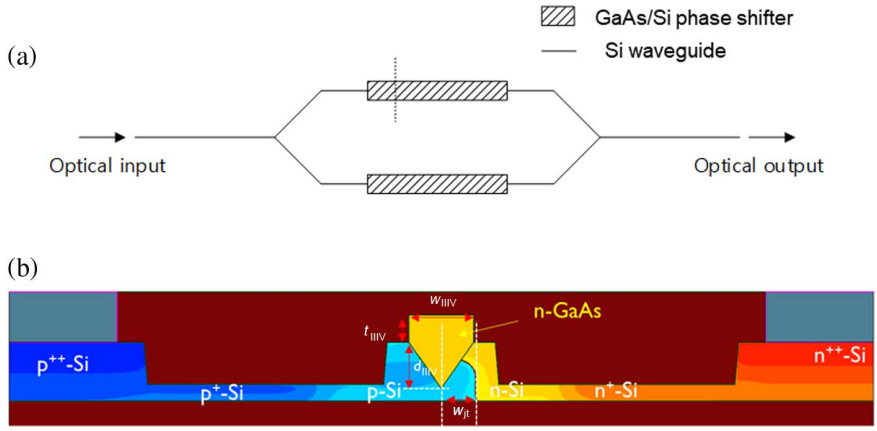

Fig. 1. (a) Schematic of a Mach–Zehnder modulator with the III–V/Si optical phase shifters in both arms. (b) Cross-section of the GaAs/Si optical phase shifter.

GaAs/Si optical phase shifter (dashed line) is shown in Fig. 1(b). Importantly, the n-type GaAs is positioned at the center of the rib waveguide, where the light is confined and propagates to promote light–matter interaction. It is electrically connected to the n-type Si on the right-hand side, and so the p-type Si/n-type GaAs and the p-type Si/n-type Si form pn junctions, which contribute optical modulation by the free-carrier plasma dispersion effect.

The device was fabricated by IMEC's CMOS line, including the monolithic selective area growth of the GaAs on the V-grooved Si trenches fabricated on a 300 mm Si-on-insulator substrate (SOI, top Si = 215 nm, buried oxide layer = 2 μm), shown in Fig. 2. The Si rib waveguide was first formed, whose widths are 450 nm for the C band application in Figs. 2(a) and 2(b). Then, ion implantation was carried out to form a pn junction in Fig. 2(c). In detail, Si regions are p-type or n-type doped, and their doping levels are very heavy (p^{++}–Si and n^{++}–Si, ~10^{20} cm^{-3}) for ohmic contact, heavy (p^{+}–Si and n^{+}–Si, ~10^{19} cm^{-3}) for low series resistance, and light (p–Si and n–Si, 5×10^{17}–10×10^{17} cm^{-3}) for optical phase shift. Then, a Si V-groove trench at the center of the Si rib waveguide was formed by wet etching in Fig. 2(d). In the waveguide center, the n-GaAs with the nominal doping density of 2×10^{18} cm^{-3} was epitaxially grown on the Si V-groove with a 100-nm-thick SiO_2 window layer in Fig. 2(e). The GaAs epitaxy on the Si V-groove was chosen to restrict the anti-phase boundaries at the interface between the GaAs/Si, which can degrade device performance [19]. Details about the GaAs growth conditions are published in Ref. [20], whereas silane was used as a Si dopant. Since the GaAs V-groove filling extended above the SiO_2 window layer, the planarization is further carried out by chemical mechanical polishing (CMP), as shown in Fig. 2(f). The GaAs width ($w_{\mathrm{III/V}}$) was the same as the Si-V groove width, 240 nm. The thickness of the GaAs in a waveguide core ($d_{\mathrm{III/V}}$) was 169 nm, which was well controlled by the anisotropic etching of the Si V-groove dependent on $w_{\mathrm{III/V}}$. The thickness of the GaAs above the Si rib ($t_{\mathrm{III/V}}$) is 70–90 nm. Finally, metal electrodes on very highly doped Si regions were constructed in Fig. 2(g). Here, it should be noted that the full process flow did not contain the wafer/die bonding process, and the electrical access to n-GaAs was designed to be realized by the epitaxial growth itself, which is a distinctive benefit of this integration process.

To investigate the layer quality of the grown n-GaAs film, we investigated the structural quality by scanning transmission electron microscopy (STEM). Figures 3(a) and 3(b) show the

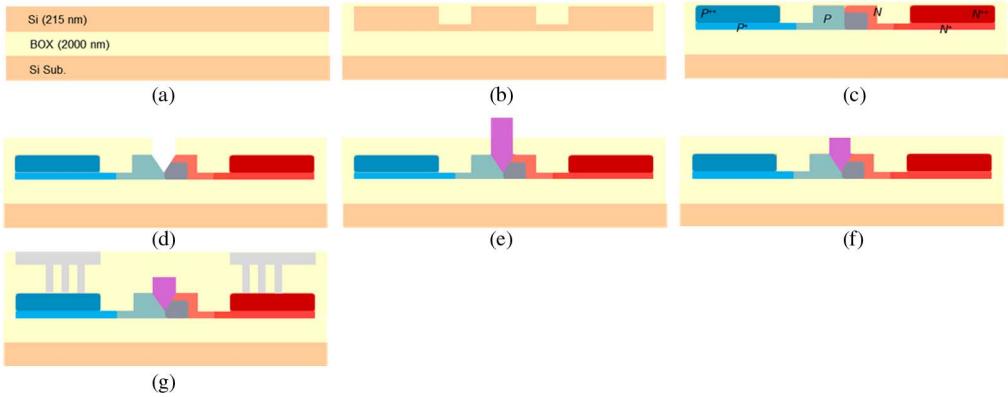

Fig. 2. Integration flow of the GaAs/Si optical phase shifter. (a) Si-on-insulator, (b) waveguide formation, (c) L-shape pn junction formation, (d) Si V-groove formation, (e) epitaxial GaAs growth on Si V-groove, (f) planarization, and (g) SiO_2 passivation and electrode formation.

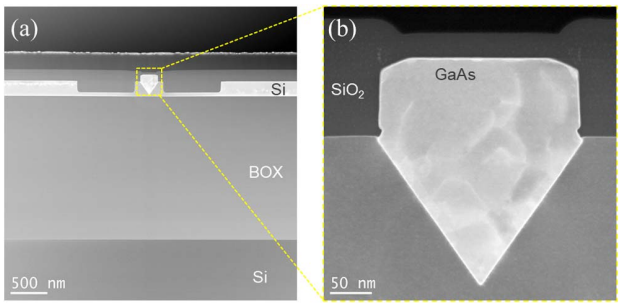

Fig. 3. (a) Cross-section of the optical phase shifter and (b) the magnified dashed yellow rectangle for GaAs/Si V-groove.

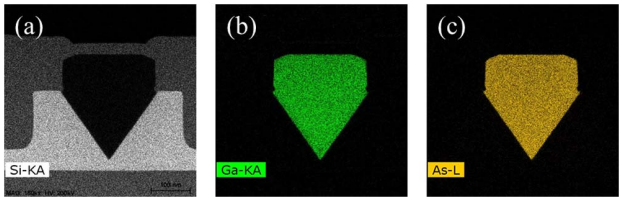

Fig. 4. EDX images of (a) Si, (b) Ga, and (c) As.

dark-field (DF) STEM image of the device cross-section and magnified image of the waveguide core, respectively. The GaAs/Si interface is clearly shown in Fig. 3(b). The bright image contrast indicates the presence of misfit dislocation in the DF-STEM picture.

It was reported before in Ref. [20] that under our chosen GaAs growth conditions a periodic array of 60° misfit dislocations is initiated along the two {111} GaAs/Si interfaces of the V-groove. This misfit array ensures the main strain relaxation and causes very bright contrast lines in the DF-STEM image. Residual strain inside the GaAs ridge leads to the nucleation of additional threading dislocations, which are also visible in the main GaAs ridge material as white contrast lines. The density of these threading dislocations clearly reduces going from the GaAs/Si interface to the GaAs ridge surface. Therefore, the crystal quality near the interface is worse than that of the top region. Figure 4 shows the energy dispersive X-ray spectroscopy (EDX) results of the GaAs on the Si V-groove region. The two-dimensional profiles of the Si, Ga, and As atoms are shown in Figs. 4(a), 4(b), and 4(c), respectively. As expected from the DF-STEM image in Fig. 3, the EDX images also show the clearly divided regions for Si and GaAs.

3. DEVICE CHARACTERISTICS

Figure 5 shows a microscopic top-view image of the fabricated lumped MZ modulators with GaAs/Si optical phase shifters. The three MZMs consist of grating couplers at the edges of both sides, two asymmetric arms with a 40-μm-length difference, optical phase shifters in both arms with three different lengths of 500, 1000, and 1500 μm, and electrodes on highly doped Si regions for both arms.

We evaluated the electrical characteristics of the pn junctions in the GaAs/Si and Si optical phase shifters. The Si optical

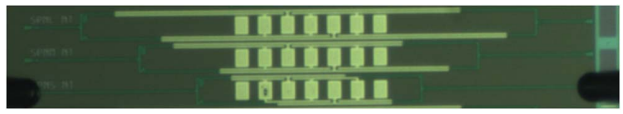

Fig. 5. Optical microscopic top-view image of the fabricated GaAs/Si V-groove lumped MZ modulators of 500-, 1000-, and 1500-μm-long optical phase shifters at both arms.

phase shifter was also characterized as a reference, which was simultaneously fabricated on the same wafer. It has a typical lateral pn junction without a V-groove and GaAs on the Si rib waveguide. Figure 6(a) shows the current-voltage (I-V) characteristics of the pn junctions for the GaAs/Si and the Si device in log scale, and the inset in the figure is plotted in linear scale. Both devices revealed rectifying properties, as expected for a pn junction diode, whereas there were several differences in the details. It is shown that the turn-on voltage of the GaAs/Si phase shifter is smaller than that of the Si phase shifter, owing to the reduction in the built-in potential by the n-GaAs/p-Si heterostructure [21]. While the leakage current of the Si device is less than ∼1 pA, the leakage current of the GaAs/Si device is not suppressed and increases as the reverse bias voltage increases. It will be caused by the misfit defects at the GaAs/Si interface where the pn junction is located. Nevertheless, the power consumption due to the leakage current ($IV_{\mathrm{rev}} \cong 1.6$ μW) is much lower compared to that due to the capacitance, $f_{\mathrm{mod}} C V_{\mathrm{rev}}^2/4 \cong 7$ mW, considering $C = 1.4$ fF/μm, $V_{\mathrm{rev}} = 2$ V, $f_{\mathrm{mod}} = 10$ GHz. Also, the GaAs/Si junction showed good rectifying behavior with a high on/off ratio exceeding at least 6 orders at ±1 V. Such defects due to misfit dislocations are inevitable for this process in order to achieve good crystal quality of the GaAs on the active area, which could be improved through defect annihilation engineering (e.g., terminating the dangling bond by hydrogen atoms) [22–25]. The forward biased current was also very high, implying that the electrical connection between n-GaAs and n-Si was very conductive, and controlling the electrical potential in the n-GaAs was successfully carried out by the one-step epitaxial growth on the Si pn V-groove. Figure 6(b) shows the measured capacitance-voltage (C-V) characteristics. As the reverse bias voltage increases across the pn junctions, the depletion width becomes wide, so the capacitance decreases. The capacitance of the GaAs/Si is much larger than that of the Si. One reason is the larger junction area of the GaAs/Si V-groove compared to the Si's lateral pn junction, as depicted in the inset of Fig. 6(b). Additionally, another reason would be a higher electron density in the GaAs than expected. We think it could be due to Si diffusion across the GaAs/Si interface into the GaAs material increasing the doping or the crystal quality of the GaAs at the interface, since the dislocation could act as a donor [26]. For high-speed performance of a depletion type modulator, the capacitance should be designed by taking the intrinsic 3-dB bandwidth of the device, $f_{3\,\mathrm{dB}} = 1/(2\pi RC)$, into account [27]. The estimated intrinsic 3-dB bandwidth of the GaAs/Si device is 16–35 GHz, considering bias dependent C_j, 1.4 and 0.65 fJ/μm at 0 to −2 V and $R_s \cong 7$ Ohm · mm from the experiment, and the TCAD simulation, respectively. Therefore,

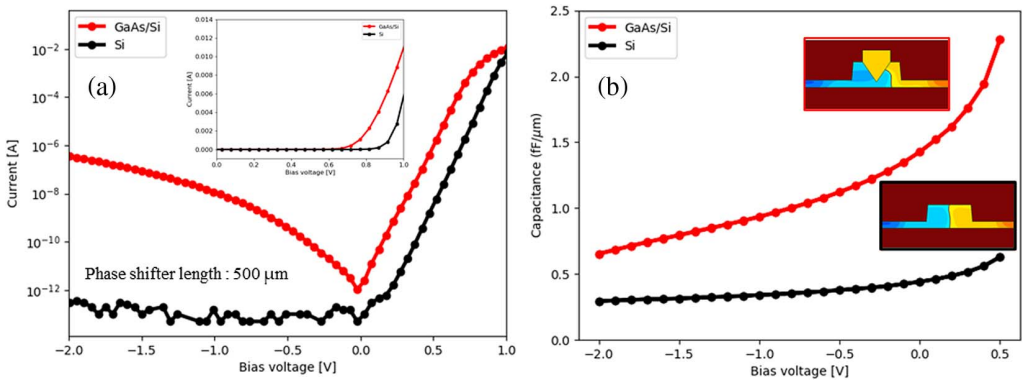

Fig. 6. Electrical characteristics of the pn junction in the GaAs/Si and Si optical phase shifters: (a) current-voltage and (b) capacitance-voltage.

it will be promising for the high-speed optical modulator applications.

For electro-optic characteristics, we measured the transmission of both lumped MZ modulators, applying the DC bias voltages shown in Fig. 7. In Fig. 5, continuous-wave transverse magnetic (TE)-polarized light in the wavelength range of 1530–1580 nm was coupled to the grating coupler on the wafer through a cleaved optical fiber. Then, the output power was measured similarly at the different bias points of the forward bias (0.5 V to the reversed bias, −2.0 V with 0.5 V steps). In addition, we measured the spectrum of a passive Si reference waveguide (REF waveguide in Fig. 7) with input and output grating couplers to remove the grating coupler dependence on a spectrum. The free spectrum range of the asymmetric MZ interferometer was designed to be approximately 15 nm via a 40 μm difference in the length between the two MZ interferometer arms. Figures 7(a) and 7(b) show the transmission spectra of the Si and the GaAs/Si modulators with various bias voltages, respectively. The 3-dB multimode interference splitters are well designed so that we can observe more than 30-dB power differences between constructive and destructive interference.

The wavelength spectra shifted with the increasing bias voltage, resulting in the increase of the optical phase difference between the two Mach–Zehnder interferometer (MZI) arms due to the plasma dispersion effect. Notably, the GaAs/Si device shows a much larger spectrum shift than the Si pn device, indicating a much efficient phase shift at the same bias conditions, which is attributed to the stronger free-electron effects in the n-GaAs. On the other hand, as seen in the spectra between the REF waveguide and MZ modulators, the insertion loss of the GaAs/Si modulator is slightly higher than that of the Si reference modulator by the difference between the spectra of the REF waveguide and the MZ modulators. We will discuss the main causes later, which are the two possible losses from the phase shifter and waveguide transitions from the Si to the GaAs/Si waveguide.

For quantitative analysis, the phase shift was extracted from these shifts in the spectra. Figure 8 shows the extracted optical phase shift and modulation efficiency of $V_\pi L$ as a function of the bias voltage. Here, $V_\pi L$ is the product of the voltage and phase shifter length for a π-phase shift. In Fig. 8(a), the circles are extracted values from the fitted spectrum, and the dashed lines are fitted curves. As expected from the larger spectrum shift of the GaAs/Si modulator compared to the Si reference modulator, the phase shift is much larger. From the fitted function, we estimated $V_\pi L$, as shown in Fig. 8(b). The $V_\pi L$ values were successfully reduced to 0.31 V·cm by introducing a monolithic GaAs/Si hybrid structure from 0.78 V·cm in reference to the Si pn modulator. This allows us to realize a shorter optical phase shifter thanks to the higher modulation efficiency of the GaAs/Si.

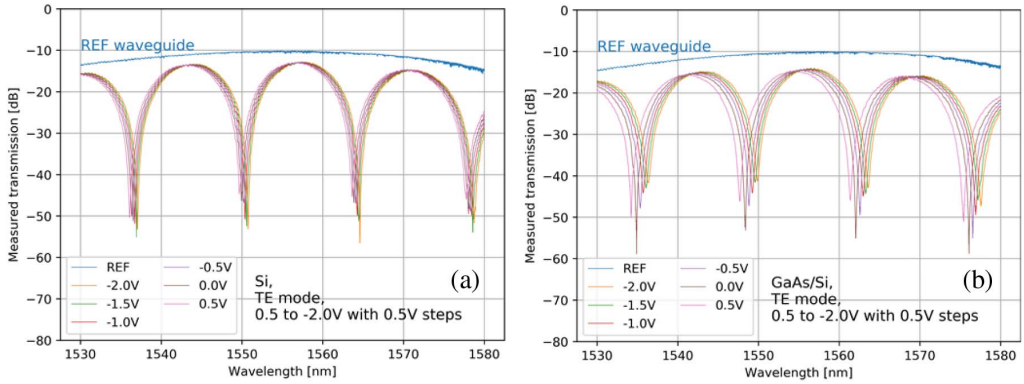

Fig. 7. Bias-dependent measured spectra of the lumped MZ modulators with the 500-μm-phase shifter length: (a) the Si reference and (b) the GaAs/Si.

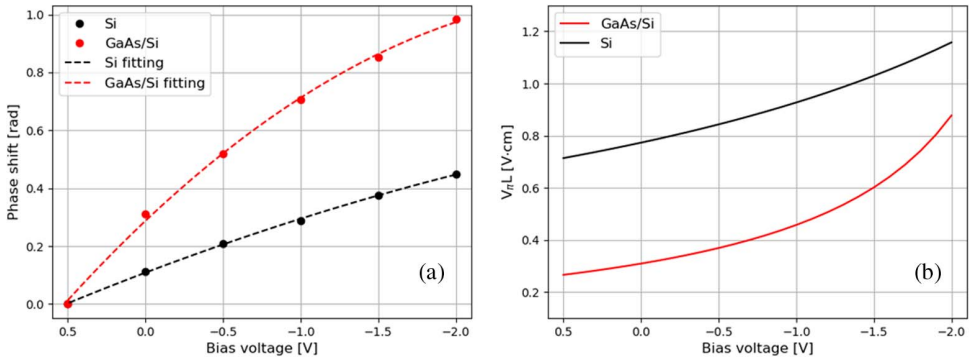

Fig. 8. (a) Extracted phase shift and (b) $V_\pi L$ as a function of the bias voltage for the GaAs/Si and the Si reference optical phase shifters.

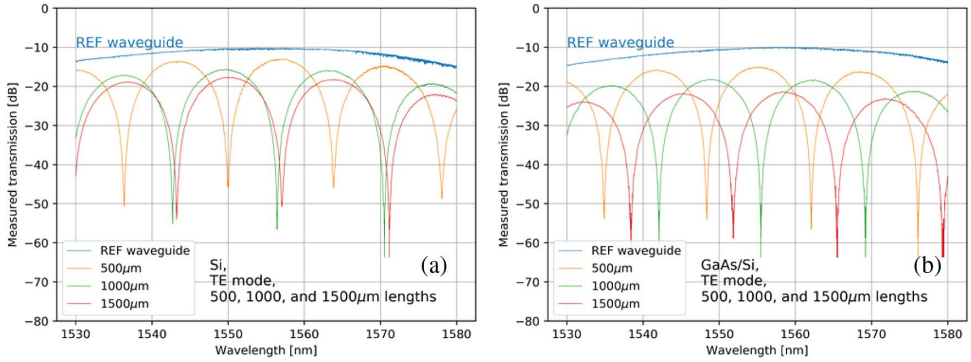

Fig. 9. Phase shifter length-dependent measured spectra of the lumped MZ modulators with 500-, 1000-, and 1500-μm phase shifter lengths: (a) the Si reference and (b) the GaAs/Si.

To characterize the phase shifter loss, we measured the transmission spectra of the MZ modulators with three different phase shifter lengths, 500, 1000, and 1500 μm, to estimate a propagation loss of an optical phase shifter. Figures 9(a) and 9(b) show the spectra for Si and GaAs/Si, respectively. The transmissions show clear interference patterns and power dependency on the lengths. By increasing the length, the insertion loss increases due to the optical loss in the phase shifter. The increase in the insertion loss of the GaAs/Si device is larger than that in the Si device, indicating higher propagation loss of the GaAs/Si compared to the Si.

The propagation loss was extracted from the slope of the normalized insertion loss as a function of the length, as shown in Fig. 10. Here, the normalized insertion loss is given by the difference between transmissions at 1550 nm of the Si REF waveguide and the MZMs. The extracted propagation losses are 6.46 dB/mm for the GaAs/Si and 4.54 dB/mm for the Si, respectively. Since the amount of the implantation dose in the pn junction formation was larger than in the conventional Si optical phase shifter (~1.6 V · cm, ~1.5 dB/mm) [28], the propagation loss is higher, whereas the $V_\pi L$ was much lower than in the conventional Si optical phase shifter. This was designed to achieve low $V_\pi L$, consequently sacrificing a propagation loss in a trade relationship [28]. Compared to our expectation based on the TCAD simulation [18], the Si

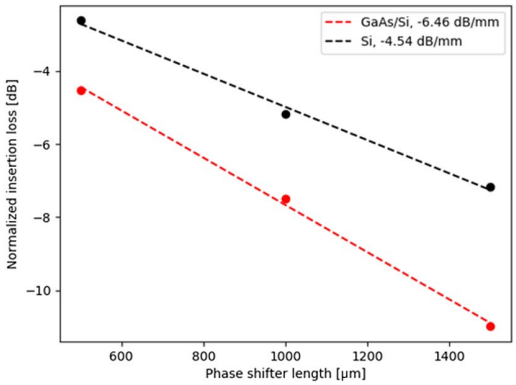

Fig. 10. Normalized insertion as a function of the phase shifter length for extracting the propagation loss of the GaAs/Si and the Si reference phase shifters.

propagation loss was reasonable for the dose conditions with the nominal doping density of 1×10^{18} cm^{-3} for p-Si and 6×10^{17} cm^{-3} for n-Si in the rib waveguide. However, the propagation loss is much higher for the GaAs/Si optical phase shifter while the $V_\pi L$ of 0.31 V · cm is close to our expectation. It could be caused by material absorption, which mainly contributes to optical loss arising from dislocation-induced energy

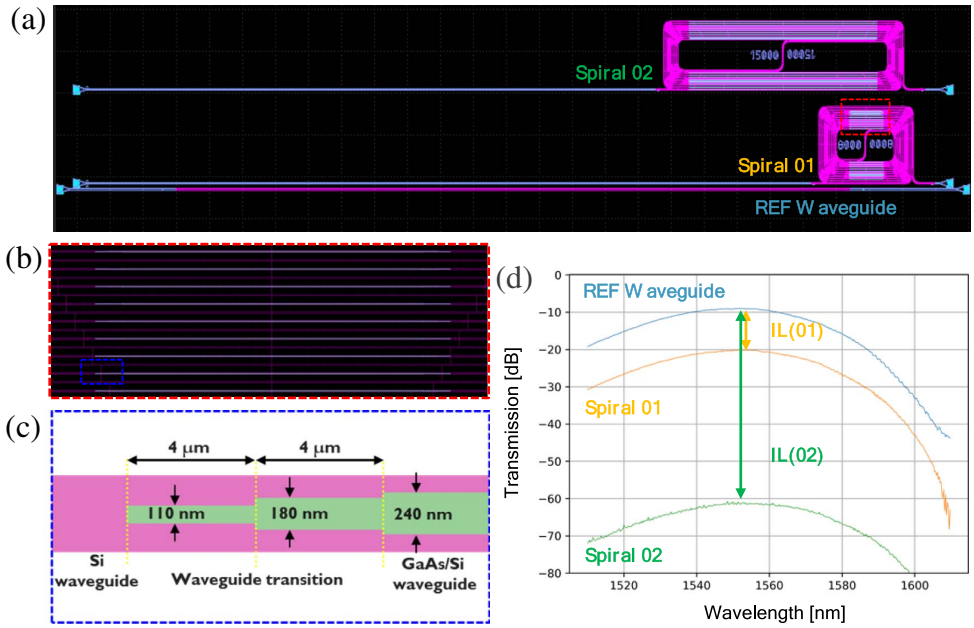

Fig. 11. (a) Test site of the spiral waveguides including the GaAs/Si waveguide, the Si waveguide, and the waveguide transition. (b) The GaAs/Si waveguide region, red-colored rectangle. (c) The waveguide transition region from the Si to the GaAs/Si waveguide, blue-colored rectangle. (d) The measured transmission of the REF waveguide, Spiral 01, and Spiral 02.

states [29]. It will be important to optimize the crystal quality of the GaAs on the Si for low dislocation density so that the propagation loss can be reduced. Also, it can be further improved by defect annihilation engineering [22–25]. If the GaAs crystal can be optimized, the propagation loss is expected to be in the range of 2.5 to 3.0 dB/mm [18].

To extract the waveguide transition loss, we measured the test site including a reference waveguide (REF waveguide) and spiral waveguides (Spiral 01 and Spiral 02), as shown in Fig. 8(a). In Spiral 01 and Spiral 02, the GaAs/Si waveguides are included, and one of them is indicated by a red-colored rectangle. Here, the GaAs/Si waveguide is the same as the GaAs/Si V-groove phase shifter, but the Si is not doped the same as the phase shifter, indicating no free-carrier absorption induced optical loss due to the boron and phosphorus implantation like the phase shifter. The enlarged image of Fig. 11(a) is shown in Fig. 11(b). As it can be seen, the GaAs/Si waveguide is included. Figure 11(c) shows the waveguide transition from Si to GaAs/Si waveguides, which is the blue-colored part in Fig. 11(b). It consists of the 8-μm-long discrete taper. Figure 11(d) is the measured transmission of the three waveguides. The insertion loss (IL) and the transmission difference between the REF and the spiral waveguides, IL(01) and IL(02) in the figure, can be expressed as

$$\mathrm{IL} = \alpha_{\mathrm{GaAs}} \times l_{\mathrm{GaAs}} + \alpha_{\mathrm{Si}} \times l_{\mathrm{Si}} + \mathrm{IL}_{\mathrm{WT}} \times n_{\mathrm{WT}}, \quad (1)$$

where α_{GaAs} and α_{Si} are propagation losses, and l_{GaAs} and l_{Si} are the lengths for the GaAs/Si and Si waveguides, respectively, and $\mathrm{IL}_{\mathrm{WT}}$ and n_{WT} are the insertion loss and the number of the waveguide transitions. The measurement result of α_{Si} is 0.115 dB/mm. Table 1 shows the known parameter values of the GaAs/Si and Si waveguide lengths and the number of waveguide transitions for Spiral 01 and Spiral 02. Since we have two spirals and one REF waveguide, we can extract two values of the unknown parameters, α_{GaAs} and $\mathrm{IL}_{\mathrm{WT}}$. We characterized it in wafer scale, and the result is shown in Fig. 12. The propagation loss is 4.9 dB/mm, and the insertion loss is 0.12 dB. Considering the difference between the phase shifter and the waveguide losses, the GaAs mostly affects the loss as much as ~75%, which should be improved by defect annihilation

Table 1. Parameter Values of Waveguide Lengths and Number of Waveguide Transitions for Spiral 01 and Spiral 02

	l_{GaAs} [μm]	l_{Si} [μm]	n_{WT}
Spiral 01	1561	6439	36
Spiral 02	9990	5010	36

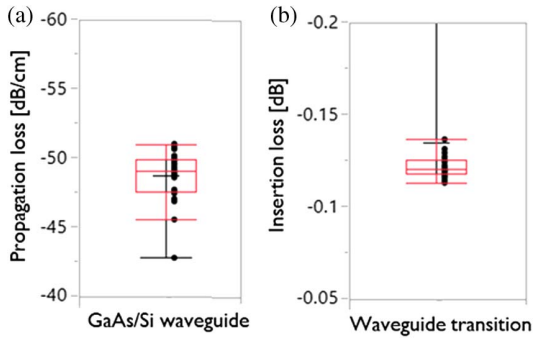

Fig. 12. (a) Propagation loss of the GaAs/Si waveguide and (b) the insertion loss of the waveguide transition.

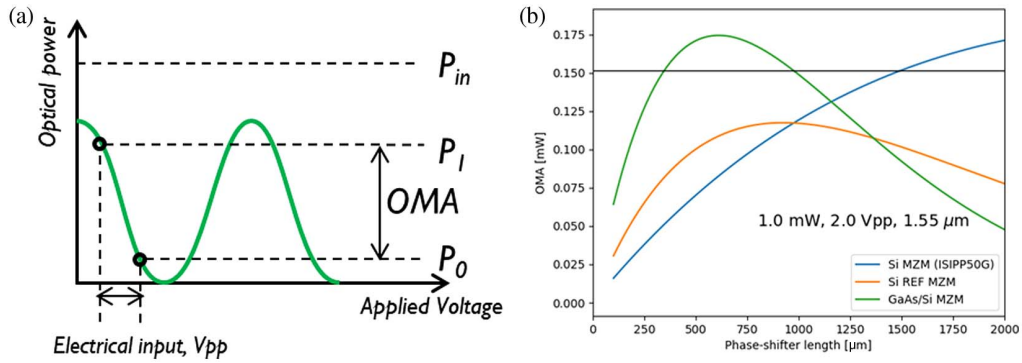

Fig. 13. (a) Optical power versus applied voltage for the OMA definition and (b) the comparison of the OMA versus the phase shifter length between the GaAs/Si and the Si modulators.

engineering. In spite of that, the GaAs/Si V-groove approach enables very low waveguide transition coupling loss.

To estimate the performance of the optical modulator, the optical modulation amplitude (OMA) is an important parameter, considering both parameters of the $V_\pi L$ and the phase shifter loss, as shown in Fig. 13(a). It is defined as the power difference ($P_1 - P_0$) considering the phase shifter loss, input optical power (P_{in}), and the peak-to-peak bias voltage (V_{pp}) across the quadrature point [30]. Figure 13(b) presents the OMA as a function of the phase shifter length for GaAs/Si and Si optical modulators. We benchmarked the fabricated GaAs/Si and Si modulators to the typical Si MZ modulator ($V_\pi L$: 1.56 V · cm, phase shifter loss: 1.38 dB/mm) [28]. We used the OMA of 0.152 mW as a target because it can be obtained by the PDK modulator with a 1.5-mm phase shifter length with the conditions of 1-mW P_{in}, $2V_{\text{pp}}$, and 1.55-μm wavelength. The Si REF MZ modulator cannot reach the OMA value because of low efficiency and high loss. Even though the loss is higher for the GaAs/Si than for the Si modulator, the OMA value can be achieved with only ∼350 μm phase shifter length, thanks to its high modulation efficiency. In terms of the energy per bit ($E_{\text{bit}} = CV_{\text{pp}}^2/4$, where C is the capacitance, and V_{pp} is the peak-to-peak voltage [31]), the GaAs/Si and Si devices are comparable, 0.49 pJ/bit and 0.495 pJ/bit respectively, considering $C = 1.4$ fF/μm, $L_{\text{phase shifter}} = 350$ μm, $V_{\text{pp}} = 2$ V for the GaAs/Si device, and $C = 0.33$ fF/μm, $L_{\text{phase shifter}} = 1500$ μm, $V_{\text{pp}} = 2$ V for the Si REF device. Therefore, it is important to notice that the length of the phase shifter can be reduced by the factor of ∼4.2 for the same optical modulation amplitude using GaAs/Si V-groove heterogeneous integration.

4. CONCLUSION

In this paper, we demonstrated monolithically integrated n-GaAs/p-Si depletion-type optical phase shifters fabricated on a 300 mm wafer-scale Si photonics platform. We characterized Mach–Zehnder modulators with the GaAs/Si optical phase shifters on both arms. They show 0.3 V · cm $V_\pi L$ modulation efficiency, much lower than that of the conventional carrier-depletion Si optical phase shifters. Although the phase shifter loss is relatively high, ∼6.5 dB/mm, it would be improved by defect annihilation engineering. In addition, the waveguide transition loss from the Si to the GaAs/Si waveguides is as low as 0.12 dB, which illustrates the potential of the GaAs/Si V-groove approach for integration into a standard Si photonics platform with low transition coupling loss. The device length is expected to be reduced by the factor of ∼4.2 for the same optical modulation amplitude of the Si Mach–Zehnder modulator thanks to the high modulation efficiency of the GaAs/Si optical phase shifter.

Funding. IMEC's industry affiliation R&D program; National Research Foundation of Korea; Ministry of Science and ICT, South Korea (2021R1G1A1091912).

Acknowledgment. The EDA tool was supported by the IC Design Education Center (IDEC), Korea.

Disclosures. The authors declare no conflicts of interest.

Data Availability. Data underlying the results presented in this paper are not publicly available at this time but may be obtained from the authors upon reasonable request.

REFERENCES

1. Y. Kim, J.-H. Han, D. Ahn, and S. Kim, "Heterogeneously-integrated optical phase shifters for next-generation modulators and switches on a silicon photonics platform: a review," Micromachines **12**, 625 (2021).
2. A. Rahim, A. Hermans, B. Wohlfeil, D. Petousi, B. Kuyken, D. van Thourhout, and R. G. Baets, "Taking silicon photonics modulators to a higher performance level: state-of-the-art and a review of new technologies," Adv. Photon. **3**, 024003 (2021).
3. C. Xiong, D. M. Gill, J. E. Proesel, J. S. Orcutt, W. Haensch, and W. M. J. Green, "Monolithic 56 Gb/s silicon photonic pulse-amplitude modulation transmitter," Optica **3**, 1060–1065 (2016).
4. P. Dong, X. Liu, S. Chandrasekhar, L. L. Buhl, R. Aroca, and Y.-K. Chen, "Monolithic silicon photonic integrated circuits for compact 100^+ Gb/s coherent optical receivers and transmitters," IEEE J. Sel. Top. Quantum Electron. **20**, 150–157 (2014).
5. T. Thiessen, P. Grosse, J. Da Fonseca, P. Billondeau, B. Szelag, C. Jany, J. K. S. Poon, and S. Menezo, "30 GHz heterogeneously integrated capacitive InP-on-Si Mach–Zehnder modulators," Opt. Express **27**, 102–109 (2019).
6. T. Hiraki, T. Aihara, K. Hasebe, K. Takeda, T. Fujii, T. Kakitsuka, T. Tsuchizawa, H. Fukuda, and S. Matsuo, "Heterogeneously integrated III–V/Si MOS capacitor Mach–Zehnder modulator," Nat. Photonics **11**, 482–485 (2017).

7. T. Hiraki, T. Aihara, T. Fujii, K. Takeda, Y. Maeda, T. Kakitsuka, T. Tsuchizawa, and S. Matsuo, "Integration of a high-efficiency Mach-Zehnder modulator with a DFB laser using membrane InP-based devices on Si photonics platform," Opt. Express **29**, 2431–2441 (2021).
8. J.-H. Han, F. Boeuf, J. Fujikata, S. Takahashi, S. Takagi, and M. Takenaka, "Efficient low-loss InGaAsP/Si hybrid MOS optical modulator," Nat. Photonics **11**, 486–490 (2017).
9. Q. Li, J.-H. Han, C. P. Ho, S. Takagi, and M. Takenaka, "Ultra-power-efficient 2 × 2 Si Mach-Zehnder interferometer optical switch based on III–V/Si hybrid MOS phase shifter," Opt. Express **26**, 35003–35012 (2018).
10. Q. Li, C. P. Ho, S. Takagi, and M. Takenaka, "Optical phase modulators based on reverse-biased III-V/Si hybrid metal-oxide-semiconductor capacitors," IEEE Photon. Technol. Lett. **32**, 345–348 (2020).
11. M. Takenaka, J.-H. Han, F. Boeuf, J.-K. Park, Q. Li, C. P. Ho, D. Lyu, S. Ohno, J. Fujikata, S. Takahashi, and S. Takagi, "III–V/Si hybrid MOS optical phase shifter for Si photonic integrated circuits," J. Lightwave Technol. **37**, 1474–1483 (2019).
12. B. R. Bennett, R. A. Soref, and J. A. Del Alamo, "Carrier-induced change in refractive index of InP, GaAs and InGaAsP," IEEE J. Quantum Electron. **26**, 113–122 (1990).
13. N. Waldron, C. Merckling, L. Teugels, P. Ong, S. A. U. Ibrahim, F. Sebaai, A. Pourghaderi, K. Barla, N. Collaert, and A. V.-Y. Thean, "InGaAs gate-all-around nanowire devices on 300 mm Si substrates," IEEE Electron Device Lett. **35**, 1097–1099 (2014).
14. C. I. Ozdemir, Y. De Koninck, D. Yudistira, N. Kuznetsova, M. Baryshnikova, D. Van Thourhout, B. Kunert, M. Pantouvaki, and J. Van Campenhout, "Low dark current and high responsivity 1020 nm InGaAs/GaAs nano-ridge waveguide photodetector monolithically integrated on a 300-mm Si wafer," J. Lightwave Technol. **39**, 5263–5269 (2021).
15. Z. Wang, B. Tian, M. Pantouvaki, W. Guo, P. Absil, J. Van Campenhout, C. Merckling, and D. Van Thourhout, "Room-temperature InP distributed feedback laser array directly grown on silicon," Nat. Photonics **9**, 837–842 (2015).
16. Y. Shi, Z. Wang, J. Van Campenhout, M. Pantouvaki, B. Kunert, and D. Van Thourhout, "Monolithic InGaAs/GaAs multi-QWs DFB nano-ridge laser directly grown on 300 mm Si wafer," in *Advanced Photonics 2017* (2017), paper ITu2A.2.
17. Y. Kim, S.-H. Kim, Y. Ban, S. Lardenois, D. Yudistira, M. Pantouvaki, and J. Van Campenhout, "Proposal and simulation of a low loss, highly efficient monolithic III–V/Si optical phase shifter," in *16th International Conference on Group IV Photonics (GFP)* (2019), paper WP29.
18. S. Kim, Y. Kim, Y. Ban, M. Pantouvaki, and J. Van Campenhout, "Simulation study of a monolithic III-V/Si V-groove carrier depletion optical phase shifter," IEEE J. Quantum Electron. **56**, 6300208 (2020).
19. M. Paladugu, C. Merckling, R. Loo, O. Richard, H. Bender, J. Dekoster, W. Vandervorst, M. Caymax, and M. Heyns, "Site selective integration of III–V materials on Si for nanoscale logic and photonic devices," Cryst. Growth Des. **12**, 4696–4702 (2012).
20. W. Guo, Y. Mols, J. Belz, A. Beyer, K. Volz, A. Schulze, R. Langer, and B. Kunert, "Anisotropic relaxation behavior of InGaAs/GaAs selectively grown in narrow trenches on (001) Si substrates," J. Appl. Phys. **122**, 025303 (2017).
21. A. Georgakilas, E. Aperathitis, V. Foukaraki, M. Kayambaki, and P. Panayotatos, "Investigation of the GaAs/Si heterojunction band lineup with capacitance and current versus voltage measurements," Mater. Sci. Eng. B **44**, 383–386 (1997).
22. G. Wang, G. Y. Zhao, T. Soga, T. Jimbo, and M. Umeno, "Effects of H plasma passivation on the optical and electrical properties of GaAs-on-Si," Jpn. J. Appl. Phys. **37**, L1280–L1282 (1998).
23. G. Wang, T. Ogawa, T. Soga, T. Jimbo, and M. Umeno, "Detailed study of H_2 plasma passivation effects on GaAs/Si solar cell," Sol. Energy Mater. Sol. Cells **66**, 599–605 (2001).
24. K. C. Hsieh, M. S. Feng, G. E. Stillman, N. Holonyak, C. R. Ito, and M. Feng, "Hydrogenation and subsequent hydrogen annealing of GaAs on Si," Appl. Phys. Lett. **54**, 341–343 (1989).
25. S. J. Pearton, C. S. Wu, M. Stavola, F. Ren, J. Lopata, W. C. Dautremont-Smith, S. M. Vernon, and V. E. Haven, "Hydrogenation of GaAs on Si: effects on diode reverse leakage current," Appl. Phys. Lett. **51**, 496–498 (1987).
26. V. Swaminathan, "Defects in GaAs," Bull. Mater. Sci. **4**, 403–442 (1982).
27. M. R. Watts, W. A. Zortman, D. C. Trotter, R. W. Young, and A. L. Lentine, "Low-voltage, compact, depletion-mode, silicon Mach–Zehnder modulator," IEEE J. Sel. Top. Quantum Electron. **16**, 159–164 (2010).
28. Y. Kim, T. Jin, and Y. Bae, "A comparative simulation study on lateral and L-shape pn junction phase shifters for single-drive 50 Gbps lumped Mach-Zehnder modulators," Jpn. J. Appl. Phys. **60**, 052002 (2021).
29. E. Peiner, A. Guttzeit, and H.-H. Wehmann, "The effect of threading disclocations on optical absorption and electron scattering in strongly mismatched heteroepitaxial III–V compound semiconductors on silicon," J. Phys. Condens. Matter **14**, 13195–13201 (2002).
30. F. Boeuf, J.-H. Han, S. Takagi, and M. Takenaka, "Benchmarking Si, SiGe, and III–V/Si hybrid SIS optical modulators for datacenter applications," J. Lightwave Technol. **35**, 4047–4055 (2017).
31. D. A. B. Miller, "Energy consumption in optical modulators for interconnects," Opt. Express **20**, A293–A308 (2012).